Chapter 2: On Signal Detection and Noise

2.0 BOOMERANG Force Detection

Without considering how to encode the NMR *spectrum* of a sample, in this chapter we address measurement of its nuclear magnetization by using the latter to drive a given mode of a mechanical oscillator. For concreteness, we consider the case of an oscillator that couples linearly to the longitudinal magnetization of the entire sample, which we therefore invert twice per oscillator period to drive the mode. We address the specifics of cyclic inversion in BOOMERANG in Chapter 3. Here we note only that the entire magnetization of the sample is inverted, and that this magnetization decays exponentially with a time constant we shall call T_{1a}, which for many samples is ideally as long as the longest relaxation time of the spin system, T_1. In a typical experiment, the Fourier component of the oscillator's motion at the driving frequency is proportional to the sample's magnetization at the beginning of a time interval during which the oscillator is driven.

In general, the oscillator's motion is defined in terms of a mechanical coordinate in the "flexible detector" of Chapter 1 along which the sample's magnetic force acts. This is also the coordinate along which the flexible suspension's restoring forces act and along which displacements are measured. We

take the "signal" to be the magnetic force exerted by the sample at the start of the oscillator-driving or *detection* period (or, rather, the projection of this force on the measured coordinate). The goal of the detection period is to measure this value with least uncertainty.

For concreteness, we return to the uniformly magnetized spherical sample inside the magnet assembly of Figure 1.3, with its designated sensor magnet. Each of the component magnets will in principle move separately in response to forces exerted by the sample's magnetization. However, since the sensor magnet is much lighter than other magnets in the assembly by design, and since the other magnets are fixed to rigid supports, the driven mechanical mode is very nearly approximated by the harmonic motion of the sensor magnet inside its encircling annulus. Thus, in the prototype described in Chapter 3, the sensor magnet moves up and down along the symmetry axis inside an otherwise rigid magnet assembly, and the displacement, z, of the sensor magnet relative to a fiber-optic position sensor fixed to the other magnets is recorded. The signal is thus defined as the net force exerted by the sample on the sensor magnet only.

The force exerted on a magnetic dipole $\boldsymbol{\mu}_d$ by another dipole $\boldsymbol{\mu}_s$ may be written

$$\mathbf{F} = -\nabla\left(-\mathbf{B}_s \cdot \boldsymbol{\mu}_d\right) = +\nabla\left(\frac{\mu_0}{4\pi}\boldsymbol{\mu}_s \cdot \left(\frac{3\hat{\mathbf{r}}\hat{\mathbf{r}} - 1}{r^3}\right) \cdot \boldsymbol{\mu}_d\right), \tag{2.1}$$

where $\hat{\mathbf{r}}$ denotes the unit vector pointing from the position of $\boldsymbol{\mu}_s$ (the *s*ample) to that of $\boldsymbol{\mu}_d$ (the *d*etector), ∇ denotes the gradient with respect to the coordinates of

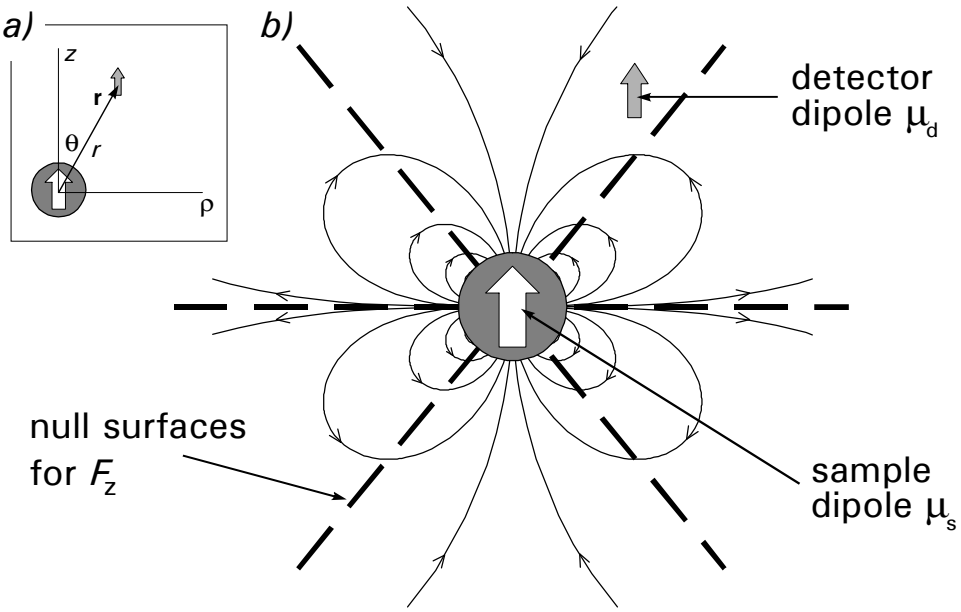

Figure 2.1. Force field near a sample with moment μ_s for axial detector dipoles μ_d. a) Coordinate system used in the text. b) Dotted lines define surfaces of revolution upon which the z-component of the force vanishes.

$\boldsymbol{\mu}_\mathbf{d}$, and $\mathbf{B}_s$ denotes the magnetic field due to the sample[1]. To calculate the force of one rigid body of finite extent on another, we must replace $\boldsymbol{\mu}_\mathbf{s}$ by $\mathbf{M}_s(\mathbf{r}_s)dV_s$ and $\boldsymbol{\mu}_\mathbf{d}$ by $\mathbf{M}_d(\mathbf{r}_d)dV_d$ and then integrate over the volumes V_s and V_d of the two bodies, whose magnetizations are $\mathbf{M}_s(\mathbf{r}_s)$ and $\mathbf{M}_d(\mathbf{r}_d)$. For the present case, $\mathbf{M}_s = M_s\hat{\mathbf{z}}$ and $\mathbf{M}_d = M_d\hat{\mathbf{z}}$ are constant vectors along the axis of cylindrical symmetry, $\hat{\mathbf{z}}$. Integration over the sample's spherical volume yields

$$\mathbf{dF} = \frac{\mu_0}{4\pi}\frac{V_s M_s M_d}{r^4}\left[\left(9-15\cos^2\theta\right)\cos\theta\hat{\mathbf{z}} + \left(3-15\cos^2\theta\right)\sin\theta\hat{\boldsymbol{\rho}}\right]dV_d \qquad (2.2)$$

for the force on the dipole element $M_d\hat{\mathbf{z}}dV_d$ at position $\mathbf{r} = r\left(\cos\theta\hat{\mathbf{z}} + \sin\theta\hat{\boldsymbol{\rho}}\right)$ in coordinates that are defined in Figure 2.1 a. Equation (2.2) may be viewed as defining a field of force around the sample that is experienced by detector dipoles

aligned along $\hat{\mathbf{z}}$. This force field is illustrated in Figure 2.1 b, where the lines of force (which are not the same as magnetic field lines) are parallel to **dF** at all points. This picture allows us to make some observations regarding the design of a suitable force detector.

First, since the force field is cylindrically symmetric, and since we wish to preserve field homogeneity in the sample volume as best as possible, our sensor magnet will be a solid of revolution about the magnetization axis $\hat{\mathbf{z}}$. Our choice of a circular cylinder, which is motivated by ease of fabrication and sample access, turns out to be very nearly the best shape (see Appendix B) given the requirement that the sensor magnet and the sample not occupy the same space. We make this latter criterion more concrete by defining a distance R_{max} from the center of the sample to the near edge of the sensor magnet. R_{max} is ideally dominated by the sample's radius, but it also includes space that may be necessary for intervening NMR coil windings and any barriers that might be required to keep the sample and sensor oscillator at different temperatures or pressures. Cylindrical symmetry requires that integration of Equation (2.2) over the sensor magnet volume yield a net force whose transverse components vanish, and so we consider only the *z*-component $dF_z = \hat{\mathbf{z}} \cdot \mathbf{dF}$ in what follows. The dotted lines in Figure 2.1 denote nodal surfaces of revolution (cones), at angles of 90° and $\theta_0 = \arccos\sqrt{3/5} \approx 39.2°$ with the vertical, upon which dF_z vanishes. The *z*-component of the force field changes sign when crossing through these surfaces. In order for the forces on individual dipole elements in the sensor to add in concert, a single, rigid sensor will lie entirely inside a nodal surface.

We calculate the dc force on the sensor magnet by integrating Equation (2.2) over the sensor's volume. The result for any volume may be written

$$F_z = \kappa_F \mu_0 V_s M_s M_d / R_{max} , \tag{2.3}$$

where

$$\kappa_F = \frac{R_{max}}{4\pi} \int \frac{1}{r^4} \left(9\cos\theta - 15\cos^3\theta\right) dV_d \tag{2.4}$$

is a dimensionless (and scale invariant) "shape factor." For a cylindrical sensor of radius *a* and height *h* placed a distance R_{max} from the center of the sample as in Figure 2.2,

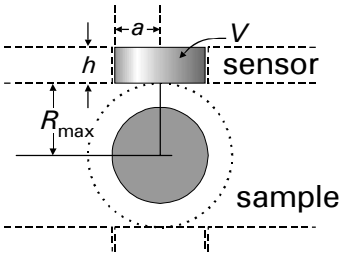

Figure 2.2. Sensor magnet dimensions and definition of R_{max}. Dotted lines denote the positions of other magnets in the BOOMERANG assembly.

$$\kappa_F = \frac{a^2 R_{max}}{2} \left(\frac{1}{\left[(R_{max} + h)^2 + a^2\right]^{3/2}} - \frac{1}{\left[R_{max}^2 + a^2\right]^{3/2}} \right). \tag{2.5}$$

2.1 Optimization of the Sensor Magnet

We consider as "optimal" the sensor magnet that maximizes the force signal-to-noise ratio,

$$SNR_{BOOM} = F_{z,rms} / F_N , \tag{2.6}$$

the ratio of the root-mean-square (rms) signal force $F_{z,rms} = \left(w/\sqrt{2}\right) F_z$, less by $\sqrt{2}$ than the dc force of Equation (2.2) and scaled by the Fourier component of the

inversion scheme used (which is $w = 4/\pi \approx 1.27$ for square-wave modulation of the longitudinal magnetization), and a time-average "noise force," F_N. The predominant noise source over a wide range of conditions is the Brownian motion of the sensor magnet. At a given temperature T, the corresponding average noise force is given by[2,3]

$$F_N = \sqrt{4k_B T \alpha \Delta f} \tag{2.7}$$

in the measurement bandwidth Δf, which is $\Delta f = 1/4T_{1a}$ in the present case[†]. The damping parameter, α, is the proportionality constant between the dissipative (frictional) force and the instantaneous velocity of the sensor magnet. This quantity may be written

$$\alpha = 2m/\tau, \tag{2.8}$$

where m is the motional mass of the oscillator, which is ideally dominated by the mass of the magnet, and where τ is the oscillator's "damping time," the time required for its amplitude to decay to $1/e \approx 36.8\%$ of its initial value after excitation by an impulse.

Empirical evidence from our prototype BOOMERANG spectrometer[4] suggests that damping due to eddy currents induced in the conducting magnets by virtue of their relative motion makes the largest contribution to the damping rate $\gamma = 2/\tau$.

[†] We define the bandwidth as $\int_0^\infty |Z(f)|^2 df \Big/ |Z(f_{max})|^2$ for a system or process with impedance or transfer function $Z(f)$ in accordance with theory[3] that leads to (2.7).

Estimates of this damping rate for the case of cylindrical symmetry are made in Appendix C. The functional form of the damping rate is complicated and not particularly instructive, and it depends much more strongly on other factors, such as the size and shape of the gap between the sensor and annulus, than it does on *a* and *h*. For that reason we leave the explicit dependence of τ on *a* and *h* out of the present optimization.

More importantly, we conclude in Appendix C that τ is scale-invariant. We write

$$\alpha = 2\left(\eta\pi a^2 h\right)/\tau \tag{2.9}$$

for the damping constant, in accordance with a motional mass dominated by a cylindrical magnet with density η. After appropriate substitutions, we then find the maximum of SNR_{BOOM} in the usual way, by differentiating Equation (2.6) with respect to both *a* and *h* and setting derivatives equal to zero. The result is a set of dimensions ($a \approx 0.59\,R_{\max}$, $h \approx 0.53\,R_{\max}$, corresponding to $\kappa_F \approx -0.072$, the sign indicating a downward force) that maximize sensitivity. It should be noted, however, that the sensitivity

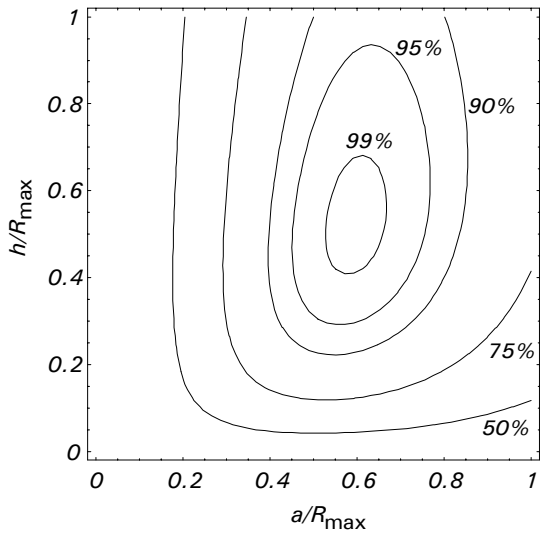

Figure 2.3. Signal-to-noise ratio (*SNR*) versus scaled radius *a* and height *h* of the sensor magnet. The contours show *SNR* relative to the *SNR* of the optimal design at $a/R_{\max} = 0.59$ and $h/R_{\max} = 0.53$. The *SNR* is not a sharply peaked function of either dimension.

figure of merit, as a function of a and h, is not sharply peaked (see Figure 2.3), and so some latitude exists in playing off sensitivity against homogeneity. The sensor magnet in Figure 2.2 is drawn with the above values for a and h relative to R_{max}.

We now turn to the scaling, relative to a linear dimension r of the sample-plus-optimized-detector, of the signal-to-noise ratio. As regards the signal, the only scale-dependent parameters appearing in Equation (2.3) are the sample's volume and R_{max}. The signal force thus scales as r^2. As regards noise, the conclusion of Appendix C, namely, the scale-invariance of the damping rate, makes α scale as r^3, and so SNR_{BOOM} is predicted to scale as $r^{1/2}$. This conclusion is based on the experimentally observed dominance of eddy-current damping at the prototype size scale. As this damping rate is scale-invariant, the $r^{1/2}$ law will hold as size scales are reduced until other mechanisms (for example, thermoelastic damping, surface losses, or so-called "anchor losses" due to phonon radiation out of mechanical supports) become more important. These damping mechanisms are the subject of much recent scrutiny in the nano-oscillator literature[5-7], and they are treated in the context of BOOMERANG by Madsen[4]. The very favorable $r^{1/2}$ scaling is in marked contrast to sensitivity scaling in inductive detection, to which we now turn.

2.2 Inductive Detection

For direct comparison to BOOMERANG, we assess sensitivity in inductive detection in the same way, by defining the signal-to-noise ratio,

$$SNR_{INDUCT} = V_{rms}/V_N , \tag{2.10}$$

in terms of a measured quantity, the rms electromotance V_{rms} in the coil, which is proportional to the magnetization of the sample. During detection, the sample's magnetization drives an electrical oscillator (an *LC* circuit tuned near the Larmor frequency of the target spins). The time-average noise voltage, V_N, is usually dominated by Johnson noise (thermal voltage fluctuations) in the resistive coil, but can also include contributions from dielectric losses in tuning capacitances and, for electrically lossy samples such as living tissue or solutions with electrolytes at physiological concentrations, induction losses in the sample. The average noise electromotance at a given temperature T is

$$V_N = \sqrt{4k_B TR\Delta f} \tag{2.11}$$

in the measurement bandwidth Δf. Here, R denotes the total resistance of the circuit at the Larmor frequency. The ohmic resistance in a conductor can be substantially larger at radio frequencies than at dc due to the skin effect, the tendency of rapidly oscillating currents to flow only within a shallow depth near the surface of a conductor. As a point of reference, the skin depth in room-temperature copper coils (with conductivity $\sigma = 5.8\times10^7\ \Omega^{-1}\text{m}^{-1}$ and permeability $\mu \approx \mu_0$) at $\omega/2\pi = 200\,\text{MHz}$ is[8]

$$\delta = \left(\frac{2}{\omega\sigma\mu}\right)^{1/2} \approx 4.7\mu\text{m}\,. \tag{2.12}$$

The bandwidth Δf of the measurement can be maximized and V_N minimized by prolonging the magnetization during detection with pulsed spin locking[9], in which the NMR circuit is driven by the sample's precessing magnetization during

the windows of a pulse sequence. Loss of magnetization then takes place exponentially with time constant $T_{1\rho}$, the rotating-frame relaxation time, which can be substantially larger than T_2, the transverse relaxation time. The bandwidth for the signal is then $\Delta f = b \times 1/4T_{1\rho}$, where the factor b, which accounts for the fact that the rf preamplifier is effectively decoupled from the signal for part of the time following pulses to avoid saturation and damage, can be substantially larger than unity. As a best case, $b = 1$ is used in the numerical examples that follow.

Since the detected signal is the electromotance induced in the detection coil by time-varying magnetization, the detector in this case is actually sampling the *electric* field induced by the sample. This fundamental detection process, the analogue of detecting the static force between two dipoles considered in section 2.0, is shown in Figure 2.4. An element of a conductor is positioned in the field of the magnetic dipoles in the sample, which are sources of electric field when they reorient in response to applied magnetic fields (*e.g.*, during precession). The electric field induced at **r** by the precessing magnetization may be obtained by taking the time derivative of the magnetic vector potential **A**(**r**) induced at **r** by a magnetic moment $\boldsymbol{\mu}_s$:

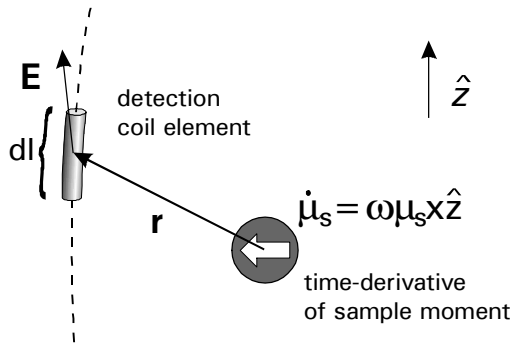

Figure 2.4. Electric field near a sample dipole with time-varying moment μ_s at the position of a detection coil element **dl**. The time-derivative vector is shown — the moment vector μ_s is out of the plane of the page for samples containing spins with positive magnetogyric ratios.

$$\mathbf{E}(\mathbf{r}) = -\frac{\partial}{\partial t}\mathbf{A}(\mathbf{r}) = -\frac{\partial}{\partial t}\left(\frac{\mu_0}{4\pi}\frac{\boldsymbol{\mu}_s \times \hat{\mathbf{r}}}{r^2}\right) = \frac{\mu_0}{4\pi}\frac{\hat{\mathbf{r}} \times \dot{\boldsymbol{\mu}}_s}{r^2} = \frac{\mu_0}{4\pi}\omega\frac{\hat{\mathbf{r}} \times (\boldsymbol{\mu}_s \times \hat{\mathbf{z}})}{r^2}. \qquad (2.13)$$

The last equality is true for magnetic dipoles precessing in the *xy*-plane perpendicular to $\hat{z}$ at angular frequency ω. For a sample of finite size, we replace $\boldsymbol{\mu}_s$ by $\mathbf{M}_s(\mathbf{r}_s)dV_s$, where $\mathbf{M}_s$ is the sample's magnetization at position $\mathbf{r}_s$ within the sample, and integrate over the sample volume dV_s. The result for a uniformly magnetized spherical sample with $\boldsymbol{\mu}_s$ along the *y*-axis is

$$\mathbf{E}(\mathbf{r}) = \frac{\mu_0}{4\pi}\omega M_s V_s \frac{\hat{\mathbf{r}} \times \hat{\mathbf{x}}}{r^2}. \qquad (2.14)$$

The electric field of Equation (2.14) can be viewed as a field of force, the analogue of the force field acting on magnetic dipoles in Figure 2.1. Here, the electric field acts on point charges, which are the electrons in the conducting coil. Figure 2.5 shows a density plot of the force field, with its strength indicated by color. The picture strongly suggests that a solenoid wound around the sample is an ideal detector.

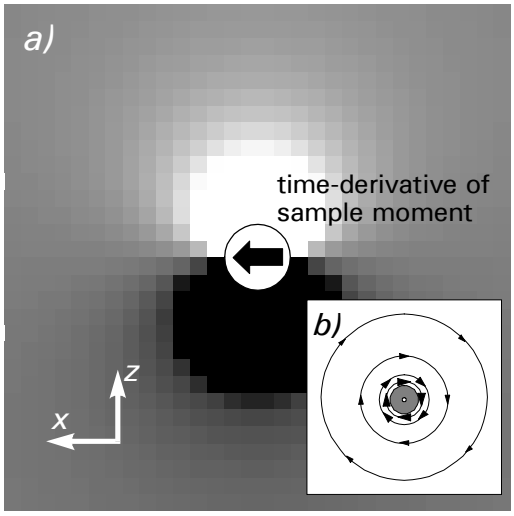

Figure 2.5. a) Density plot of the electric field near a sample with time-varying magnetization. The time derivative of the magnetization is as shown. The electric field is perpendicular to the page for all points in the plane of the page. b) View of the electric field from the side, along the axis of $\dot{\mu}_s$.

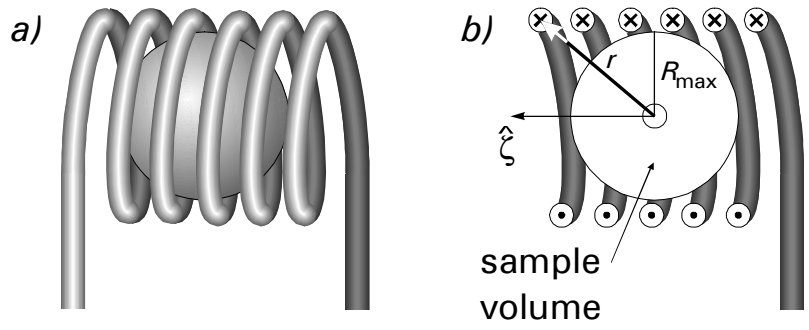

Figure 2.6. Inductive detector model. a) Sample in an NMR induction coil. b) Internal view with position **r** of the coil element defined. $\hat{\zeta}$ is a unit vector along the direction of the time derivative of the sample's magnetization.

Figure 2.6 shows a solenoidal coil wound around a spherical sample with a distance of closest approach, R_{max}, defined as shown. As in BOOMERANG, R_{max} is ideally dominated by the sample's radius, but technical considerations, such as the homogeneity of applied rf fields, can demand that R_{max} exceed the sample's radius by tens of percent and usually much more. The amplitude V of the oscillating electromotance is obtained by integrating Equation (2.14) over the coil. While the relevant integration was over a detector magnet volume in BOOMERANG, in this case, it is a line integral along a current path C:

$$V = \int_C \mathbf{E}(\mathbf{r}) \cdot \mathbf{dl} \,. \tag{2.15}$$

The result for any geometry can be written

$$V = \kappa_V \mu_0 V_s M_s \omega / R_{max} \,, \tag{2.16}$$

where

$$\kappa_V = \frac{R_{max}}{4\pi} \int \frac{\mathbf{r} \times \hat{\boldsymbol{\zeta}} \cdot \mathbf{dl}}{r^3} \tag{2.17}$$

is a shape factor for the coil, the analogue of κ_F, and $\hat{\boldsymbol{\zeta}}$ is the unit vector along $\dot{\boldsymbol{\mu}}_s$. For a helical *n*-turn coil of length 2*g* and radius r_c, the shape factor is

$$\kappa_V = \frac{nR_{max}}{\sqrt{r_c^2 + g^2}}. \qquad (2.18)$$

At sufficiently low frequencies, one could quantify resistive losses in the coil by setting

$$dR = \rho \frac{dL}{A} \qquad \text{or} \qquad dR = \rho \frac{dL}{p\delta}, \qquad (2.19a,b)$$

where ρ is the coil's resistivity and *A* it's cross-sectional area, and integrating over the length *L* of the unwound conductor. In Equation (2.19b), the cross-sectional area is replaced by an effective area $p\delta$, the product of the skin depth δ and a cross-sectional perimeter *p*. With appropriate substitutions, Equation (2.10) could then be used to optimize the dimensions of the solenoid. At commonly used radio frequencies, however, the situation is complicated by "proximity effects," the inductive and capacitive effects of currents in one part of the coil on other parts. These can be accounted for with a phenomenological proximity-effect factor[10-12] $\sigma \approx 3$. Optimization for the case of a (roughly spherical) human head yields an optimal winding geometry for a solenoid, as shown in Figure 2.7. While the size scale used in this optimization is far from the

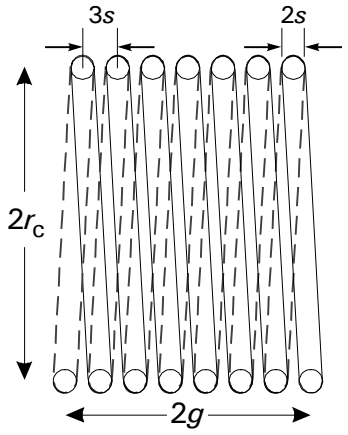

Figure 2.7. Dimensions for optimal NMR coil according to Hoult and Lauterbur[10].

microcoil designs that are our present concern, the aspect ratio $g/r_c = 0.7$ turns out to be consistent with intuition from Figure 2.5 and with results of the simpler optimization suggested above, and we shall use the dimensions of Figure 2.7 in the numerical examples that follow.

Using Equations (2.11) and (2.16), the latter reduced by the factor $\sqrt{2}$ as befits an rms electromotance, we may write Equation (2.10) as

$$SNR_{\mathrm{INDUCT}} = \frac{\kappa_V \mu_0 V_s M_s \omega / R_{\max}}{\sqrt{8 k_B T R \Delta f}}, \tag{2.20}$$

This is to be compared to the expression for BOOMERANG, which can be written

$$SNR_{\mathrm{BOOM}} = \frac{\kappa_F w \mu_0 V_s M_s M_d / R_{\max}}{\sqrt{8 k_B T \alpha \Delta f}}. \tag{2.21}$$

As we have already remarked, SNR_{BOOM} scales as $r^{1/2}$. We can similarly analyze SNR_{INDUCT}. The scale-dependent factors in the numerator of Equation (2.20) are the sample's volume and $R_{\max}$, and so we find that the signal electromotance scales as r^2. In the size regime where the coil's windings are larger than the skin depth, the resistance R, which is proportional to the conductor's total length divided by its cross-sectional perimeter, is scale-invariant. In accordance with Equation (2.20), in this regime SNR_{INDUCT} scales as r^2. At smaller scales, where current flows more uniformly through wires that are small in comparison to the skin depth, the resistance is proportional to total length and inversely proportional to cross-sectional area, and it therefore scales inversely with r. In that case SNR_{INDUCT} scales as $r^{5/2}$. These scaling relations are confirmed by the observations of Peck *et*

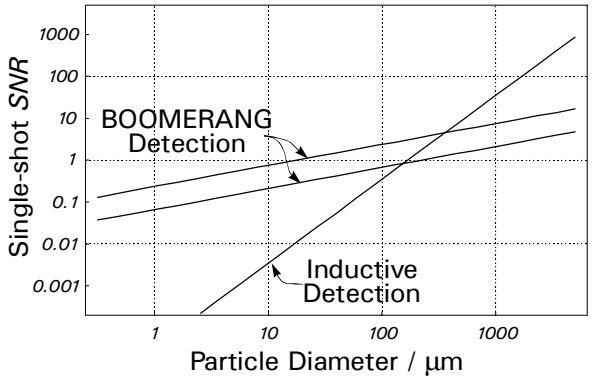

R_{max}	34 μm
sample mass	0.3 μg
# of spins	$6x10^{13}$
detector mass	0.2 μg
magnetization	2 T/μ_0
frequency	500 Hz
ring-down times	80 ms, 1 s
coil x-section	15 μm
coil diameter	83 μm
coil length	58 μm
# of turns	6

Figure 2.8 SNR and scaling for inductive detection and BOOMERANG. Signal-to-noise ratios are estimated for natural-abundance (4%) ^{29}Si NMR at 17 MHz in a 2T field at 150 K. The sample is scapolite, a siliceous mineral believed to be present in martian soil. The simulation is motivated by a study of low-power spectrometers for *in-situ* planetary exploration. The parameters at right are for the hypothetical optimized inductive and BOOMERANG detectors for a 60 μm sample, and the curves at left are based on the scaling relations described in the text. A one-second relaxation time is assumed for the magnetization, and two ring-down times are chosen for the BOOMERANG curves. The 80 ms time has been demonstrated experimentally at the millimeter scale, and, at fields higher than the 0.66 T of the prototype and with careful attention to eddy-current suppression, 1 s ring-down times are anticipated.

al., who report *SNR* per unit volume of r^{-1} and $r^{-1/2}$ in NMR experiments in microcoils with diameters above and below ~250 μm at 200 MHz (4.7 T)[13].

This prediction that SNR_{BOOM} decreases substantially more slowly with size than does SNR_{INDUCT} suggests that BOOMERANG will have superior sensitivity at and below a sufficiently small size scale. In Figure 2.8, SNR_{BOOM} and SNR_{INDUCT} are estimated and plotted over 5 orders of magnitude in sample size for a ^{29}Si NMR spectrum of the mineral scapolite. This example is motivated by a hypothetical mineralogical study with a low-power spectrometer transported to Mars on a space probe. The simulated device is optimized at each scale, and the parameters used in the simulation are listed the accompanying table.

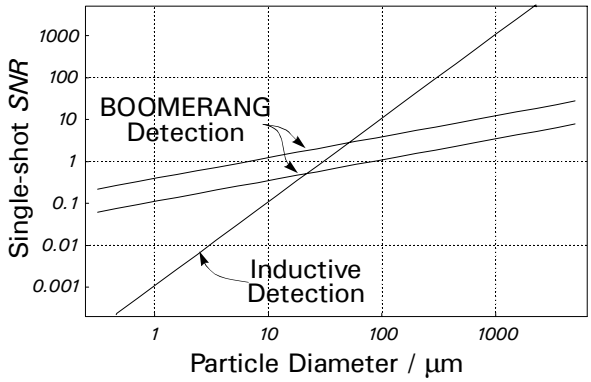

R_{max}	34 μm
sample mass	0.17 μg
# of spins	$2x10^{12}$
detector mass	0.2 μg
magnetization	2 T/μ_0
frequency	500 Hz
ring-down times	80 ms, 1 s
coil x-section	15 μm
coil diameter	83 μm
coil length	58 μm
# of turns	6

Figure 2.9 SNR and scaling in proton NMR. Signal-to-noise ratios are estimated for ^{1}H NMR at 500 MHz and 310 K. The sample is a crystal of a hypothetical 50 kD protein, and the SNR is for a single proton site per molecule, or perhaps a ^{13}C label which has been polarization-enhanced and indirectly detected. As in Figure 2.8, the parameters at right are for optimized inductive and BOOMERANG detectors for a 60 μm sample, and the curves at left are based on the scaling relations described in the text. A one-second relaxation time is assumed for the magnetization, and again 80 ms and 1 s are chosen for the oscillator ring-down times. The graphs show that, even for this case that is most favorable for inductive detection, there is a useful size range where BOOMERANG methods are predicted to exhibit superior sensitivity.

While the scaling relations apply to all nuclei, the size scale below which BOOMERANG's sensitivity is predicted to exceed that of inductive detection will depend on the magnetogyric ratio of the target spin and on the strength of the field. The Larmor frequency ω, which appears in SNR_{INDUCT} (2.20), is absent in SNR_{BOOM} (2.21), and so the relative advantage of BOOMERANG is greater at a given scale for nuclei with small magnetogyric ratios at fixed field, or at lower fields for a given nuclide. The case most advantageous to inductive detection (with the exception of NMR of tritium, whose magnetogyric ratio exceeds the proton's by 7%) is proton spectroscopy in high field. Figure 2.9 shows that, even in the 11.7 T field of a commercial 500 MHz superconducting magnet, BOOMERANG's sensitivity is preferable in samples with R_{max} below about 20-50 μm.

The foregoing motivates construction of a BOOMERANG spectrometer at the sub-millimeter scale, and efforts toward microfabrication of BOOMERANG spectrometers are detailed elsewhere[4,14]. But even with the $r^{1/2}$ scaling of SNR_{BOOM}, sensitivity is still a challenge at smaller scales, and so a proof-of-concept instrument optimized for 3 mm samples was constructed. That instrument is subject of Chapter 3.

2.3 A Note About Reciprocity

The integrand in Equation (2.15) may be interpreted in two ways. We have already used it to describe the electric field induced at the site of a conductor by a time-varying magnetic dipole. With the help of Equation (2.13), this integrand may be rewritten

$$\mathbf{E}(\mathbf{r})\cdot\mathbf{dl} = -\frac{\partial}{\partial t}\left(\frac{\mu_0}{4\pi}\frac{\boldsymbol{\mu}_s\times\hat{\mathbf{r}}\cdot\mathbf{dl}}{r^2}\right) = +\frac{\partial}{\partial t}\left(\boldsymbol{\mu}_s\cdot\frac{\mu_0}{4\pi}\frac{\hat{\mathbf{r}}'\times\mathbf{dl}}{r^2}\right) = -\frac{\partial}{\partial t}\left(\boldsymbol{\mu}_s\cdot\mathbf{d}\tilde{\mathbf{B}}_1\right) \qquad (2.22)$$

where $\hat{\mathbf{r}}' = -\hat{\mathbf{r}}$ is the unit vector pointing from the *current element* **dl** to the *sample dipole* $\boldsymbol{\mu}_s$. $\mathbf{d}\tilde{\mathbf{B}}_1$ is the element of magnetic field induced at $\boldsymbol{\mu}_s$ per unit current flowing through **dl**. We can thus recast the equations that permit us to calculate the induced electromotance by exchanging the roles of the "source" and "observation point." This is a reciprocity relationship[8]. The right-hand side of Equation (2.22) has been the standard means of calculating signal-to-noise ratios in NMR since Hoult and Richards introduced it in 1976[15]. One can calculate (or measure) a local sensitivity

to magnetic moments by integrating $\mathbf{d}\tilde{\mathbf{B}}_1$ over the NMR coil, and this can be useful in evaluating imaging apparatus.

A similar analysis can be applied to force detection. For a differential sample moment $\mathbf{d}\boldsymbol{\mu}_s$, Equation (2.1) may be written in two ways:

$$\mathbf{dF} = \nabla(\mathbf{B}_s \cdot \mathbf{d}\boldsymbol{\mu}_d) = \nabla\left(\frac{\mu_0}{4\pi}\boldsymbol{\mu}_s \cdot \left(\frac{3\hat{\mathbf{r}}\hat{\mathbf{r}} - 1}{r^3}\right) \cdot \mathbf{d}\boldsymbol{\mu}_d\right) = -\tilde{\nabla}(\boldsymbol{\mu}_s \cdot \mathbf{dB}_d) = -\boldsymbol{\mu}_s \cdot \mathbf{d}\left(\tilde{\nabla}\mathbf{B}_d\right), \quad (2.23)$$

which are related by the antisymmetry of the gradients (∇ and $\tilde{\nabla}$) of the dyadic $(3\hat{\mathbf{r}}\hat{\mathbf{r}} - 1)/r^3$ with respect to the coordinates of the detector and sample dipoles, respectively. The parameter $\mathbf{dG} = \mathbf{d}\left(\tilde{\nabla}\mathbf{B}_d\right)$ is the change in the magnetic field at the *sample* (due to the detector element $\mathbf{d}\boldsymbol{\mu}_d$) per unit displacement of the flexible detector along the "detection coordinate," *z*. That this reciprocity parameter **dG**, the equivalent of $\mathbf{d}\tilde{\mathbf{B}}_1$ in inductive detection, has units of magnetic field gradient (T/m) is an artifact of the detection coordinate's units, which are length (m) in the case we have treated here. The displacement may also be an angle, as we shall see in Chapter 5 when the subject of torsional oscillators is taken up.

References

1 G. M. Leskowitz, L. A. Madsen, and D. P. Weitekamp, *Sol. St. Nucl. Magn. Reson.* **11,** 73 (1998).

2 S. Chandrasekhar, *Rev. Mod. Phys.* **15,** 1-89 (1943).

3 C. W. McCombie, *Rep. Prog. Phys.* **16,** 266-320 (1953).

4 L. A. Madsen, Ph. D. Thesis, California Institute of Technology, 2002.

5 R. Lifshitz and M. L. Roukes, *Phys. Rev. B* **61,** 5600-5608 (2000).

6 M. L. Roukes, in *Solid-State Sensor and Actuator Workshop* (Hilton Head Island, SC, 2000).

7 K. Y. Yasamura, T. D. Stowe, E. M. Chow, T. Pfafman, T. W. Kenny, B. C. Stipe, and D. Rugar, *J. Microelectromech. Sys.* **9,** 117-125 (2000).

8 P. Lorrain, D. R. Corson, and F. Lorrain, *Electromagnetic Fields and Waves*, 3rd ed. (W. H. Freeman and Co., New York, 1988).

9 D. P. Weitekamp, *Adv. Magn. Reson.* **11,** 111 (1983).

10 D. I. Hoult and P. C. Lauterbur, *J. Magn. Reson.* **34,** 425-433 (1979).

11 B. B. Austin, *Wireless Eng. Exp. Wireless* **11,** 12 (1934).

12 F. E. Terman, in *Radio Engineer's Handbook*, 1st ed. (McGraw-Hill, New York, 1943), pp. 73-90.

13 T. L. Peck, R. L. Magin, and P. C. Lauterbur, *J. Magn. Reson. B* **108,** 114 (1995).

14 T. George, *et al*., in *IEEE Aerospace Conference* (Big Sky, Montana, 2001).

15 D. I. Hoult and R. E. Richards, *J. Magn. Reson.* **24,** 71 (1976).